Non-covalent interactions in hexanuclear polyoxidometalates [V(6)(IV)B(20)O(50)H8](8-) An experimental and theoretical approach

Karina Munoz-Becerra, Kerry Wrighton-Araneda, Eric Le Fur, Jean-Yves Saillard, Samia Kahlal, Olivier Cador, Veronica Paredes-Garcia, Diego Venegas-Yazigi

Non-covalent interactions in hexanuclear polyoxidometalates $[V^{IV}_6B_{20}O_{50}H_8]^{8-}$. An experimental and theoretical approach.

Karina Muñoz-Becerra[1¥], Kerry Wrighton-Araneda[1†], Eric Le Fur[2], Jean-Yves Saillard[3], Samia Kahlal[3], Olivier Cador[3], Verónica Paredes-García[4,5], Diego Venegas-Yazigi[*1,4]

[1]Facultad de Química y Biología, Universidad de Santiago de Chile, USACH, Av. Libertador Bernardo O'Higgins 3363, Estación Central, Región Metropolitana, Santiago, Chile.

[2]Department Univ Rennes, ENSCR, CNRS ISCR-UMR 6226 F-35000 Rennes, France

[3]Department Univ Rennes, CNRS ISCR-UMR 6226 F-35000 Rennes, France

[4]Centro para el Desarrollo de la Nanociencia y Nanotecnología, CEDENNA, Santiago, Chile

[5]Departamento de Ciencias Químicas, Universidad Andrés Bello, Santiago, Chile.

[¥]Present address: Dirección de Investigación y Postgrado, Universidad de Aconcagua, Pedro de Villagra 2265, Vitacura, Chile.

[†]Present address: Programa Institucional de Fomento a la Investigación, Desarrollo e Innovación. Universidad Tecnológica Metropolitana. Ignacio Valdivieso 2409, P.O. Box 8940577, San Joaquín, Santiago, Chile.

Supporting information for this article is given via a link at the end of the document.

Address for Correspondence:

Dr. Diego Venegas-Yazigi

E-mail: diego.venegas@usach.cl

All authors dedicate this manuscript to their colleague and friend Jean-Rene Hamon on the occasion of his 65th birthday.

Abstract: A complete study of the optical and magnetic properties of three new *{V_6-type}* polyoxidometalates $(NH_3CH_2CH_2CH_2NH_3)_4\{V_6B_{20}O_{50}H_8\}\cdot 4H_2O$ **1**, $K_2(NH_3CH_2CH_2NH_3)_{2.5}(NH_3CH_2CH_2NH_2)\{V_6B_{20}O_{50}H_8\}\cdot 2H_2O$ **2**, and $K_2(NH_3CH_2CH_2CH_2NH_3)_2(H_3O)_2\{V_6B_{20}O_{50}H_8\}\cdot 8H_2O$ **3** is presented. Using TD-DFT calculations, the assignment of the experimental UV-Visible spectra was established with four absorption bands: a higher in energy assigned to metal-to-metal charge transfer and the remaining associated principally to *d-d* transitions, demonstrating that the $\{V_6^{IV}O_{18}\}^{12-}$ ring is the principal chromophore for these systems and that the surrounding packing does not have an influence on it. On the other hand, the differences observed in the magnetic properties are caused by the influence of the non-covalent interactions between the potassium ions with some oxygen atoms of the V^{IV} coordination spheres, thus modifying the V^{IV}-V^{IV} exchange coupling. This effect was demonstrated using a simplified binuclear DFT model that predicts a higher V^{IV}-V^{IV} antiferromagnetic coupling when the K cations become closer to the oxygen bridge atoms that link the V^{IV} centres of the $\{V_6^{IV}O_{18}\}^{12-}$ ring.

Keywords: Polyoxidometalates • non-covalent interactions • magnetic properties • spectroscopic properties • DFT calculations

Introduction

Among the polyoxidometalate family, polyoxidovanadoborates (VBO) display an exceptionally rich structural chemistry. Although vanadium atoms included in these systems always adopt a base square pyramid (SP) coordination geometry, borate units enrich the structural diversity since boron can adopt both tetrahedral [BO_4] and trigonal [BO_3] geometries [1,2]. Additionally, the VBO family has attracted considerable interest because of their magnetic, electronic and catalytic properties [3,4] associated with the presence of

vanadium(IV) atoms (d^1 configuration). Recent studies of vanadoborates related to the conductivity of these materials show the importance of the nature of the crystalline packing and all interactions present in it [5–7]. The reported VBO structures are mainly composed by six, ten and twelve vanadium centres [2,6], namely the *{V_6-type}* clusters: $\{V_6B_{20}O_{50}H_n\}$ (n=0, 6, 8, 12) [8–11] and $\{V_6B_{22}O_{54}H_{10}\}$ [12]; the *{V_{10}-type}* clusters: $\{V_{10}B_{28}O_{74}H_n\}$ [13] and $\{V_{10}B_{28}O_{74}H_n\}$ (n=4, 8) [14,15]; the *{V_{12}^{i}-type}* clusters: $\{V_{12}B_{16}O_{58}H_8\}$ [16–20] and $\{V_{12}B_{17}O_{58}H_8\}$ [21]; the *{V_{12}^{ii}-type}* clusters: $\{V_{12}B_{18}O_{60}H_n\}$ (n=3, 6) [11,20,22–36], and the *{V_{12}^{iii}-type}* clusters: $\{V_{12}B_{32}O_{84}H_8\}$ [38,39]. The most interesting feature of the boron rich structures *{V_6-type}*, *{V_{10}-type}* and *{V_{12}^{iii}-type}* is their central oxo-vanadium ring formed by penta-coordinated vanadium units [VO_5]. The magnetic properties, which have shown an antiferromagnetic nature in all cases, along with their optical properties, are expected to be dependent principally on the number and oxidation state (V^{IV}/V^{V} ratio) of the interacting V atoms part of these rings. For the hexanuclear *{V_6-type}* systems reported in the literature, the authors claim that vanadium atoms are in a 4+ oxidation state [8–10,12], and only one exception of a $5V^{IV}/1V^{V}$ mixed-valence cluster have been informed by Y. Shan et. al. [11]. Despite the reported studies concerning the structural and magnetic properties of compounds of the V_6-family, until now, no evidence has been given to explain systematically the differences and similarities experimentally observed of their magnetic properties. Moreover, no detailed investigations concerning the nature of the electronic transitions and no theoretical studies can be found for the study of the non-covalent interactions present in the crystalline systems. The present work reports the syntheses, crystalline structures, UV-Visible spectra and magnetic properties of three new *{V_6-type}* compounds, $(NH_3CH_2CH_2CH_2NH_3)_4\{V_6B_{20}O_{50}H_8\}\cdot 4H_2O$ **1**, $K_2(NH_3CH_2CH_2NH_3)_{2.5}(NH_3CH_2CH_2NH_2)\{V_6B_{20}O_{50}H_8\}\cdot 2H_2O$ **2**, and $K_2(NH_3CH_2CH_2CH_2NH_3)_2(H_3O)_2\{V_6B_{20}O_{50}H_8\}\cdot 8H_2O$ **3**, all based on the $\{V_6B_{20}O_{50}H_8\}^{8-}$ polyanion. Using DFT and TD-DFT calculations, we provide for the first time a theoretical

rationalization of the experimental magnetic and UV-Visible properties of *{V_6-type}* polyoxidometalates. A complete experimental-theoretical analysis is presented to explain their magnetic and optical properties. The results allow us to prove the importance of the crystalline arrangement over the magnetic behaviour dominated by the V^{IV}-V^{IV} coupling in the hexanuclear V_6-ring at low temperature and its negligible impact over the UV-Vis electronic properties.

Materials and methods

All chemicals were reagent grade and used without further purification.

Synthesis

Compounds **1** – **3** were obtained using boric acid flux in a Parr reactor.

$(NH_3CH_2CH_2CH_2NH_3)_4\{V_6B_{20}O_{50}H_8\}\cdot 4H_2O$ **1.** A mixture of V_2O_5 (1 mmol, 0.182 g), H_3BO_3 (25 mmol, 1.5453 g) and 1,3-diaminopropane (6 mmol, 0.500 mL), in a molar ratio of 1:25:6, was added into a 23 mL Teflon lined Parr reactor and heated at 180°C for 3 days. After cooling to ambient temperature, the final solid mixture was washed with hot water (60°C) to remove the excess of boric acid, obtaining a pure phase of light green crystals. These were dried at room temperature (Yield: 53% based on V).

$K_2(NH_3CH_2CH_2NH_3)_{2.5}(NH_3CH_2CH_2NH_2)\{V_6B_{20}O_{50}H_8\}\cdot 2H_2O$ **2.** A mixture of KVO_3 (1 mmol, 0.1384 g), H_3BO_3 (25 mmol, 1.5453 g) and ethylenediamine (6 mmol, 0.402 mL), in a molar ratio of 1:25:6, was added into a 23 mL Teflon lined Parr reactor and heated at 180°C for 3 days. After cooling to room temperature, the final solid mixture was washed with hot water (60°C) to remove the excess of boric acid, obtaining **2** as a pure phase of light green crystals. (Yield: 57% based on V).

$K_2(NH_3CH_2CH_2CH_2NH_3)_2(H_3O)_2\{V_6B_{20}O_{50}H_8\}\cdot 8H_2O$ **3.** A mixture of KVO_3 (1 mmol, 0.1384 g), H_3BO_3 (25 mmol, 1.5453 g) and 1,3-diaminopropane (6 mmol, 0.500 mL), in a molar ratio of 1:25:6, was added into a 23 mL Teflon lined Parr reactor and heated at 180°C for 3 days. After cooling to room temperature, the final solid mixture was washed with hot water (60°C), obtaining a pure phase of light green crystals (Yield: 63% based on V).

In each synthesis, the alkyl-diamine added in excess to the vanadium source acts as a reducing agent allowing the change of vanadium(V) to vanadium(IV) that forms the $\{V_6^{IV}O_{18}\}^{12-}$ rings, as has been proved before [26]. To determine the structure of the final crystalline materials, FT-IR, elemental analysis (C, N, and H), and X-Ray powder and single crystal diffraction measurements were done (these analyses were done only for the final crystalline products of **1** – **3**).

Equipment and Characterization Techniques

Crystal Structure Determination. Data collection for **1** and **3** were performed at room temperature on a Bruker-Kappa-CCD diffractometer with graphite-monochromatized Mo-Kα radiation (I = 0.71073 Å). Intensities were collected employing the program COLLECT [40]. Data collection for **2** was recorded at room temperature on a Bruker Smart Apex diffractometer, using separations of 0.3° between frames and 10 s by frame. Data integration were made using SAINTPLUS [41]. Reflection indexing, Lorentz polarization correction, peak integration, and background determination were carried out with the DENZO program of the Kappa-CCD software package [42]. Unit-cell parameters refinement and frame scaling were performed with the program DIRAX/LSQ [43]. Data integration and scaling of the reflections were performed with the suite SCALEPACK [44]. The structures were solved by direct methods using XS in SHELXTL [45] and completed (non-H atoms) by Fourier difference synthesis. Refinements until convergence was obtained using XL SHELXTL [46] and SHELXL97 [47]. The H-atom positions were calculated after each cycle of

refinement using a riding model, with C—H = 0.97 Å and Uiso(H) = 1.2 Ueq(parent) and N—H = 0.89 or 0.91 Å and Uiso(H) = 1.5 Ueq(parent). Crystal data, structure refinement, bond distances and angle values are given in Table S1 to S3 in the SI for the studied compounds.

Elemental Analysis. The analysis of compounds **1** – **3** were done to corroborate the purity of the bulk samples analysed. The elemental analyses were performed in a Thermo-Fisher Flash 1112 elemental analyser.

UV-visible Spectra. KBr pellets suitable for IR were used for UV-visible absorption spectra. Absorption spectra were recorded at room temperature on a Varian Cary 5000 UV-visible-NIR spectrometer equipped with an integrating sphere accessory.

FT-IR Spectroscopic Measurements. IR spectra of **1** - **3** were recorded on a Perkin Elmer FT-IR spectrophotometer, model BX II, from 4000 to 400 cm^{-1} using KBr pellets**.** The detailed assignment of the FT-IR absorption bands of all compounds is given in the supporting information.

Powder X-Ray diffraction. P-XRD experiments of crystalline samples were carried out in Bruker D8 Advance diffractometer employing a linear detector.

Magnetization Measurements. The magnetization measurements were obtained on a polycrystalline sample previously analysed by powder X-ray diffraction to confirm the presence of the same phases as the diffracted single crystal. Measurements were done in the temperature range of 2 – 300 K using a Quantum Design MPMS-XL5 SQUID magnetometer with an applied dc field of 2 kOe (2 to 20 K) and 10 kOe (20 to 300 K). Diamagnetic corrections were estimated from Pascal constants [48].

Electronic Paramagnetic Resonance Spectroscopy Measurements (EPR). EPR measurements were recorder for solids of **1** – **3** using a Bruker EMX-1572 spectrometer in

the temperature range of 270 and 130 K under N_2 liquid flux, working at a frequency = 9.35 Hz (X-band).

Computational Details. DFT calculations were carried out using the Gaussian09 code revision D.02 and its standalone programs [49]. Calculations were performed using the hybrid functional B3LYP [50,51]. The triple-ζ Ahlrich orbital basis set (TZV) [52] was employed to represent the orbital structure. Dispersion force corrections for self-consistent field energies were considered with DFT-D3 method developed by Grimme et al [53]. The spin-unrestricted open-shell model assuming their maximum electronic multiplicity (S=3) were considered imposing the non-symmetric restriction. To improve the electronic descriptions of the polyanion, the continuum solvated model based on density (SMD) [54] using water (Ɛ=78) was considered in all cases, as is demonstrated by Lopez *et al.* for polyanions with high negative overall charges [55–57]. The vibrational analysis was carried out to confirm that the structure was optimized at the global minimum in energy. TD-DFT calculations [58–60] allowed assigning the experimental UV-Visible spectra for each studied species. For these purposes, 250 electronic transitions were considered with the non-symmetry restriction. The assignment based on the electronic structure was obtained at the same theory level of the optimization. Additionally the hybrid B3PW91 [51,61] and PBE0 [62–64] functional were tested in the TD-DFT calculations. The conceptual framework of the hole-electron theory applied to the molecular system, included in the MultiWFN 3.3.8 package [65], supports the electronic transition assignment and permits to graphically render the molecular orbitals implicated on each considered transition, represented as hole-electron density surfaces. The magnetic modelling was developed using a vanadium(IV) binuclear simplified model based on a crystal structure. The theoretical magnetic constants coupling were calculated using the broken-symmetry approach [66,67]. Quadratic algorithm convergence with tight criteria was used to converge the antiferro/ferromagnetic

configurations. The Heisenberg-Dirac-Van Vleck spin Hamiltonian was used for the exchange coupling:

$$\hat{H} = -\sum_{i>j} J_{ij} \hat{S}_i \cdot \hat{S}_j$$

In the above, S_i and S_j are the spin operators of the paramagnetic centres *i*, *j* of the V^{IV} dimmer. J_{ij} exchange magnetic coupling constant was obtained using the broken symmetry approach:

$$E_{HS} - E_{BS} = -(2S_1S_2 + S_2)J$$

where E_{HS} and E_{BS} correspond to the total energy of high-spin and broken-symmetry states that represent ferromagnetic and antiferromagnetic states, respectively. The terms S_1 and S_2 are the total spins of the involved paramagnetic centres considering $S_1 \geq S_2$, being $S_1 = S_1 = ½$ for vanadium. Finally, the graphical interface used to represent the structures and molecular orbitals was the ChemCraft 1.8 package [68].

Results and Discussion

Structural description

The relative purity and crystallinity of the phases were confirmed by comparing the theoretical and experimental powder X-Ray diffraction pattern given in the supporting information. Elemental analyses also show good agreement between experimental and calculated (see supporting information). The crystalline lattices of the three compounds are based on the $\{V_6B_{20}O_{50}H_8\}^{8-}$ polyanion, formed by a central oxo-vanadium hexagonal ring $\{V_6O_{18}\}^{12-}$ composed by six edge-sharing penta-coordinated vanadium centres, each one adopting a SP coordination geometry, as is depicted in the polyhedral representation in Figure 1. Each vanadium atom of the ring is slightly displaced towards the axial position with τ values ranging from 0° to 4°, thus, being almost undistorted [69,70]. The O-V-O basal

angles of each [VO_5] moiety are lower than 180°, ranging between 139.85° and 143.47° for **1**, 138.81° and 143.16° for **2**, and 139.05° and 142.12° for **3**. The V···V non-bonding distances are close to 3.0 Å, and the intracluster cavity diameters ($V_i – V_i'$) are very similar in all cases, with values close to 6.1 Å (Table S1). In all the *{V_6-type}* polyanions the $\{V_6O_{18}\}^{12-}$ ring is bonded to two equivalent polyborate ligands of formula $\{B_{10}O_{22}H_4\}^{10-}$ (Figure 1), each containing a central tetrahedral [BO_4] moiety bonded to other six [BO_4] units through three oxygen atoms, leaving the fourth as a terminal protonated B-OH group. The six tetrahedrons are bridged alternately with trigonal [BO_3] borate units that share two of its oxygen atoms with two internal [BO_4] entities, having the third protonated {$HOBO_2$}. The B-O bond lengths (and the O-B-O angles; ~120° for [BO_3] and ~109° for [BO_4]) of the borate ligands $\{B_{10}O_{22}H_4\}^{10-}$ in are in the expected normal range [1,39] (Table S1). It is important to recall that during the Difference Fourier map at the final stage of structure completion, a remaining electronic density was assigned to a water molecule in the inner cavity of each polyanion $\{V_6B_{20}O_{50}H_8\}^{8-}$ in **2** and **3**. Protonated diamines compensate the negative charge of the *{V_6-type}* polyanions in **1**, and by potassium cations and protonated diamines in **2** and **3** to reach the electro-neutrality of each crystalline system. Besides, these counterbalance ions produce a stabilizing effect in the crystalline lattice by hydrogen bonds and by electrostatic interactions with the terminal oxygen atoms of the polyanions. In particular, the intercluster space in **1** is occupied by diprotonated 1,3-propanodiamine molecules (1,3-diapH_2) along with water solvation molecules. The 1,3-diapH_2 cations are found in two different crystallographic sites and present hydrogen bonds with terminal and bridging oxygen atoms from the $\{V_6B_{20}O_{50}H_8\}^{8-}$ anion, forming thus a three-dimensional network (Figure S1). Besides, the $\{V_6B_{20}O_{50}H_8\}^{8-}$ are interacting with each other by hydrogen bonds between the terminal protonated trigonal {$HOBO_2$} units (B7–O18···O14=2.765(4) Å; B9–O24···O19=2.889(4) Å; B4–O13···O17=2.632(4) Å) increasing the stabilization of the pseudo-3D crystalline packing (Figure S1). The crystalline packing of **2** and **3** can be

explained considering the two-dimensional lamellar arrangement along the *ac* plane (Figures S2-S3), in which there are two potassium cations per formula occupying only one crystallographic site. Each potassium is octa-coordinated and connects three vanadoborate anions, while the tetranuclear K–(O_2)–K unit connects four polyanions, producing the lamellar *ac* growth of the structures (Figure S4). In these two compounds, the potassium coordination environment has the same nature: linked to the same oxygen-bridge (B–O–B and V–O–B) and terminal oxygen atoms (O_2B–O and V–O_t) from the $\{V_6B_{20}O_{50}H_8\}^{8-}$ anions (Figure 2, Figure S4, and Table S2). An RMSD (root mean square deviation) value of 0.008 obtained by evaluating the metric parameters of the two binuclear K-O-K units of compounds **2** and **3** proves that they have a very similar structural disposition of the K-O-K unit within their crystalline packing. Since compound **2** presents the highest disorder for the diamine cations and water molecules, its crystalline packing showing only the clusters and the potassium cation is represented in Figure S2. Additional to the potassium cations, the crystalline network of **3** (Figure S3) contains crystallization water molecules and diprotonated 1,3-propanediamine (1,3-diapH_2) cations, which are in one crystallographic site and produce a pseudo-three-dimensional lattice by hydrogen bonds with the polyanions. The calculated average bond valence sum (BVS) [71] for vanadium atoms were obtained for the four compounds with values of 4.055 for **1**, 4.083 for **2**, and 4.092 for **3**. These experimental values are very close to the expected value of 4 considering that the vanadium atoms are V^{IV} centres, with one unpaired *d* electron.

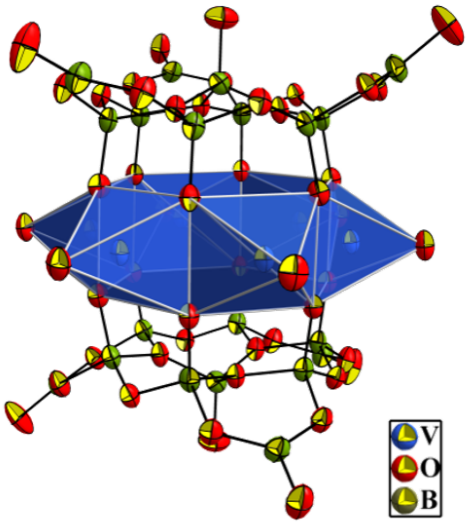

Figure 1. The $[V_6B_{20}O_{50}H_8]^{8-}$ polyanion, showing the central $[V_6O_{18}]$ ring as polyhedral representation. Atomic displacement ellipsoids at the 50% probability level and hydrogen atoms omitted for clarity.

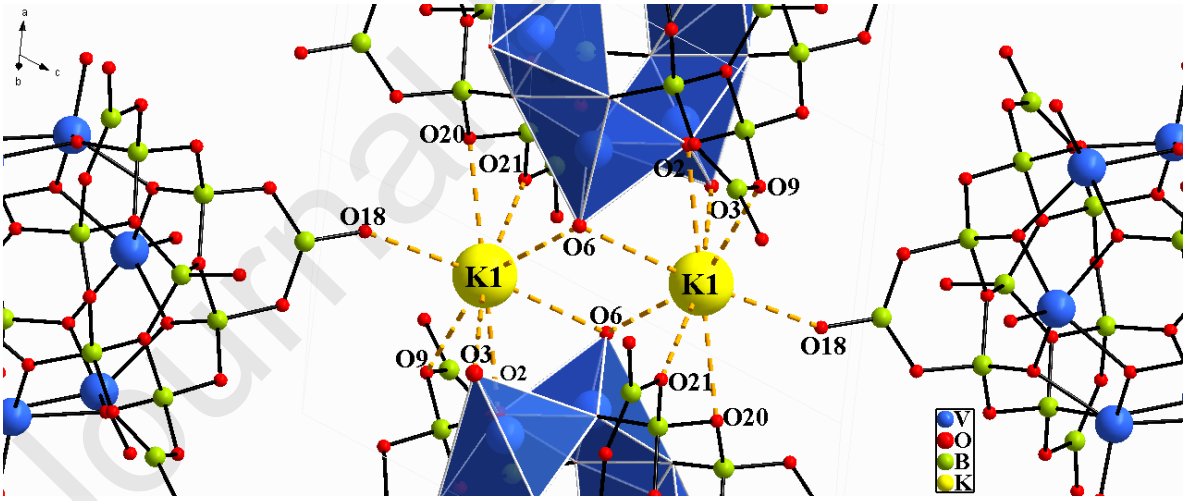

Figure 2. The binuclear K–(O_2)–K unit for **2** and **3**, connecting four $[V_6B_{20}O_{50}H_8]^{8-}$ polyanions. The octa-coordinated environment of each K atom is shown with dotted lines. The interacting vanadyl groups are depicted in polyhedral representations (the atoms labels are referred to compound **3**).

Infrared spectroscopy

The vanadyl stretching band ($\nu_{V\text{-}Ot}$) appears at c.a. 920 cm^{-1} for all studied compounds and in the expected range [9,10,14,16–19,21,22,26,27–32,37,71-73]. However, compounds **2** and **3** show a broad band with a shoulder, while compound **1** shows a narrower band than the former ones (Figure 3). This fact can be rationalized considering the interactions that some vanadyl groups present in the different crystalline lattices: whereas compound **1** has only protonated amines in the lattice, which are interacting through hydrogen bonds with oxygen atoms from vanadyl and borate fragments, compounds **2** and **3** only have interactions of some vanadyl groups with potassium cations. Thus, the broad band with a shoulder for the vanadyl stretching vibration shows that all vanadyl groups are not equivalent. It is important to recall that the donor-acceptor distances are smaller for the N(amine)-O(borate) than the N(amine)-O(vanadyl) interactions; therefore, it is expectable that the vanadyl stretching vibration in the FT-IR spectrum of compound **1** should present a narrower band. The full range FT-IR spectra for **1** – **3** with the corresponding assignments are given in the supporting information.

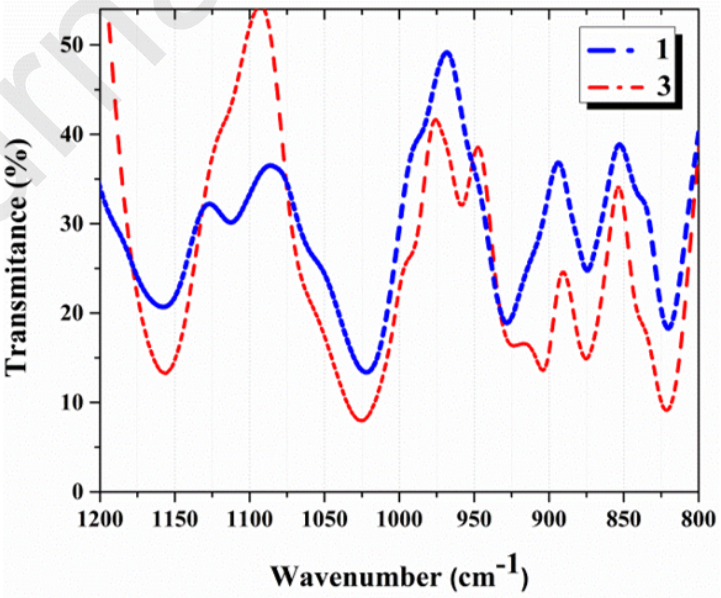

Figure 3. Selected infrared spectra of **1** and **3** in the 800 – 1200 cm^{-1} region. The spectrum for compound **2** is like that of **3** (see supporting information).

Magnetic properties

Variable-temperature magnetic measurements in the temperature range of 2 to 300 K were carried out for **1** – **3**. Table 1 summarizes the negative *Θ* values obtained from the corresponding $\chi_M^{-1}(T)$ curves, evidencing a bulk antiferromagnetic behaviour for the three compounds. In Figure 4, the χ_MT(T) plot for the studied compounds is shown. For **2** and **3** a subtle χ_MT decrease is observed in the range of 300 to 100 K, more noticeable for **1**. Below 100 K the χ_MT curves decrease abruptly, which is typical for an antiferromagnetic behaviour. The experimental χ_MT values per (V^{IV}) centre at room temperature are 0.334, 0.312, and 0.344 emu·mol^{-1}·K for **1**, **2**, and **3**, respectively (Table 1). These values are very similar to the calculated spin-only value of 0.342 emu·mol^{-1}·K and 0.349 emu·mol^{-1}·K for one V^{IV} centre with S=1/2, considering the experimental g values of 1.91 for **1**, and 1.93 for **2** and **3**, respectively, showing that there are differences in the crystal field of the vanadium centres (data obtained from EPR spectroscopy, Figure 5). The calculated Curie Constants (*C*) per V^{IV} centre at 300 K listed in Table 1 are in the range of the *C* calculated considering one unpaired electron (C= 0.342 for **1** with g=1.91 and C=0.349 for **2** and **3** with g=1.93). The effective magnetic moment values (μ_{eff}) obtained at 300 K (Table 1) for one unpaired electron are similar to those obtained theoretically (μ_{eff}= 1.600 for **1**, and μ_{eff}=1.651 for **2**, **3**). These obtained parameters indicate that the three compounds are slightly antiferromagnetically coupled (V^{IV}, *s* =1/2) in the high-temperature range. Based on the above described structural characteristics of **1** – **3**, the magnetic coupling between the vanadium(IV) atoms in the polyanions is mainly influenced by the crystalline arrangement of each compound and is slightly affected by the geometry differences of the V^{IV} centres in the V_6*-rings*. This was

confirmed by evaluating each VO_5 polyhedron of each compound using SHAPE software [75] (Table S7). Therefore, the different magnetic responses are mainly attributed to the different interactions between the counterbalancing cations of each crystalline system with the *V_6-type* polyanions. It is important to point out that many factors are ruling the magnetic response of the compounds. The effective magnetic moment varies with the magnitude of the crystal field and the magnitude of the exchange interactions. The latter is being influenced by the non-covalent interactions in the crystal packing. As it is possible to observe in Figure 4, **1** and **3** (with 1,3-diapH_2 cations in **1**, and K and 1,3-diapH_2 cations in **3**) are less coupled at room temperature, while **2** is more coupled, having K and diammonium cations as counterbalancing ions. In this sense, it has been demonstrated before that K cations have a direct influence over the magnetic V^{IV}-V^{IV} coupling through V=O···K [2,26]. For **3** it is possible to see that the effect of both K and 1,3-diapH_2 cations produces a quenching on the exchange, while the presence of only 1,3-diapH_2 cations in **1** allows inferring that the pure hydrogen bonds interactions with the *V_6-type* polyanions allow a more favourable magnetic interaction compared to that of **3** (that also includes K cations). This fact permits us to conclude that along with the crystalline arrangement of each compound, the nature of the non-covalent interactions present in the lattices affects the magnetic exchange of the clusters. Experimental EPR spectra measured in the range of 270 and 130 K for **1 – 3** are shown in Figure 5. The different obtained g values are indicative of differences between the crystal field on the spin-carriers, which can be due to the non-covalent interactions. It is observed that the hyperfine structure of **1** is more defined than for **2** and **3**, which indicates a less electronic delocalization of the d^1 electrons of the V^{IV} paramagnetic centres for **1**. Contrarily, in **2** and **3** a higher d^1 electronic delocalization could be inducing the low hyperfine resolution. In the χ_MT(T) plot of Figure 4, within the range of 300 to 100 K, **1** shows a subtle decrease of the curve, being softer for **2** and **3**. This fact implies that **1** requires less thermal order than **2** and **3** to reach the antiparallel spin-coupling between the

V^{IV} centres, leading to populating the lowest spin state (S=0). The above-described magnetic behaviour can be related with the crystalline packing of **2** and **3**, specifically with their similar binuclear K-O-K units (see Table S5), indicating an evident influence of the non-covalent interactions between these counterbalancing units on the V^{IV}-V^{IV} magnetic interactions as well on the Fermi contact of each V^{IV} centre.

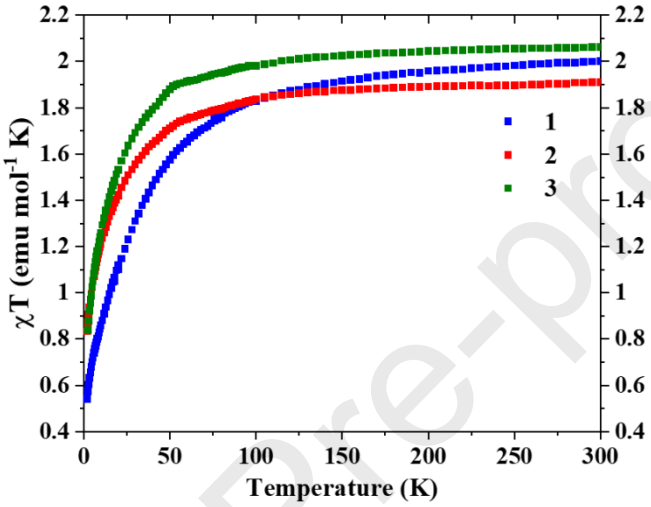

Figure 4. Temperature dependence of χ_MT for **1**, **2**, and **3**.

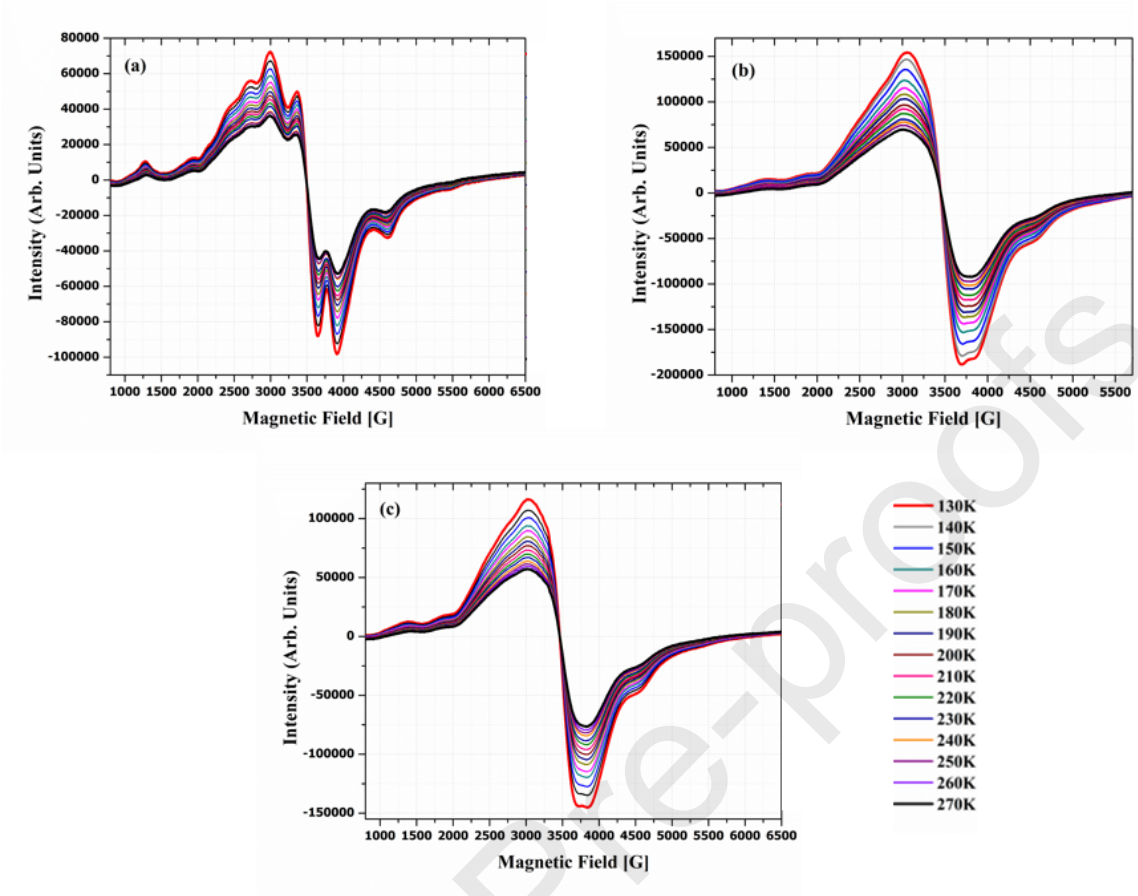

Figure 5. EPR spectra for compounds (a) **1**, (b) **2**, and (c) **3**, measured between 270 K and 130 K. The spectra were obtained under a N_2 liquid flux (frequency = 9.35 Hz).

Table 1. Experimental values of $\chi_M T$ and the effective magnetic moment (μ_{eff}) per V^{IV} centre at 285K for **1**, **2**, and **3**.

	Crystalline system	χT (emu mol^{-1} K) (285 K)	C (emu mol^{-1} K) (285 K)	μ_{eff} (BM) (285 K)	C /per V^{IV} center	Θ (K)
1	$(NH_3CH_2CH_2CH_2NH_3)_4\{V_6B_{20}O_{50}H_8\} \cdot 4H_2O$	2.001	2.096	1.617	0.349	-14.25
2	$K_2(NH_3CH_2CH_2CH_2NH_3)_{2,5}(NH_3CH_2CH_2CH_2NH_2)\{V_6B_{20}O_{50}H_8\} \cdot 2H_2O$	1.872	1.903	1.593	0.317	-5.57
3	$K_2(NH_3CH_2CH_2CH_2NH_3)_2(H_3O)_2\{V_6B_{20}O_{50}H_8\} \cdot 8H_2O$	2.061	2.099	1.652	0.350	-5.48

Besides, magnetic data were fitted by using PHI program [76] adopting the isotropic Hamiltonian (H_{iso}) given by the equation:

$$H_{iso} = -\sum_{i=1, j\neq i}^{6} J_i \hat{S}_i \cdot \hat{S}_j + \beta \sum_{i=1}^{6} \hat{S}_i \cdot g_{exp}$$

where β and g_{exp} parameters are the Bohr magneton and the experimental *g*-factor obtained from EPR measurements. The model employed identifies three exchange coupling constants J_1, J_2, and J_3, in accordance with the crystallographic asymmetric unit of the $\{V_6B_{20}O_{50}H_8\}$ cluster that contains three vanadium(IV) centres (Table S2-S4). The obtained fits (Figure S6 and Table S6) display a general tendency described as below:

- for the three compounds **1** – **3**, J_1 and J_2 present an antiferromagnetic nature being $J_1 \approx 3J_2$,
- J_3 displayed a ferromagnetic interaction for compounds **2** and **3** that contain K ions in their crystalline structure, while for compound **1**, J_3 displays a low antiferromagnetic nature,
- for the most significant antiferromagnetic coupling constant J_1 (see Table S6), the tendency follows J_1(**1**) > J_1(**2**) > J_1(**3**), which suggest that the presence of K cations in **2** and **3** affect the magnetic V^{IV}-V^{IV} exchange, decreasing their antiferromagnetic coupling.

Electronic properties

The absorption spectra in the solid-state for **1** – **3** are shown in Figure 6. For each compound, four bands in the range of 300 to 1000 nm are observed: the lower energy band (band-I) appears in the range of 690 and 710 nm; band-II is observed in 515 to 530 nm range, followed by band-III at 415 to 425 nm; the higher energy band (band-IV) is in the range of 300 to 315 nm (Table S8). The similar shapes of the three spectra suggest that the optical properties of these crystalline networks are principally given by the {*V_6-chromophore*}=$\{V_6^{IV}O_{18}\}^{12-}$ of the VBO clusters.

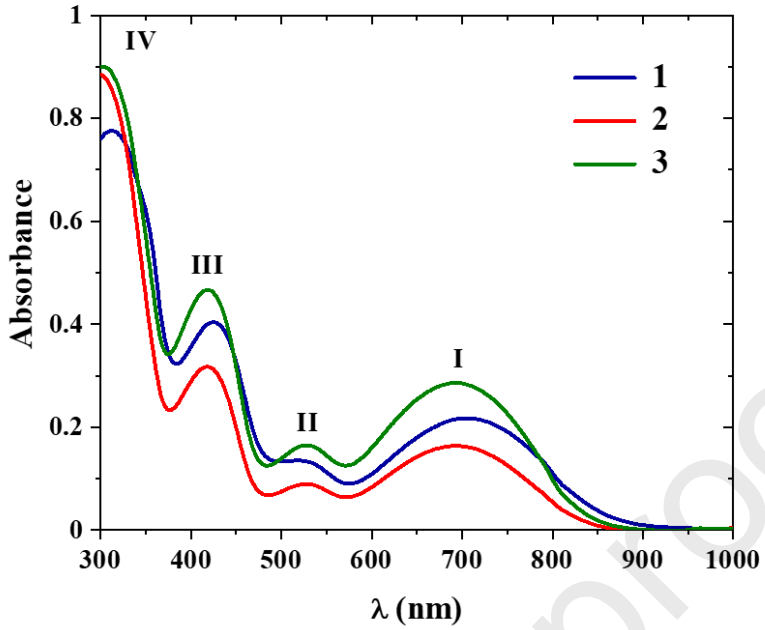

Figure 6. Solid state absorbance UV-visible spectra of **1** – **3** (see Table S8).

Theoretical studies

Binuclear V^{IV} model: the influence of K on the magnetic properties of 2 and 3.

Considering that in **2** and **3** the non-covalent K-O interactions that link two adjacent V_6-polyanions (Figure 2) were associated with their magnetic differences, a binuclear V^{IV} model was constructed to evaluate the influence of the K cations over the magnetic V^{IV}-V^{IV} superexchange (Figure 7a). Crystallographically, each system's shorter K···O distance is associated with an oxygen atom that bridges the V^{IV}-V^{IV} pairs in each cluster (Table S5). Based on this observation, we have varied the K···O distance of one K cation positioned onto the plane formed by bridging oxygen atoms that connects the vanadium(IV) centres in the model system. We evaluated the variation of the magnetic V^{IV}-V^{IV} coupling constant (J) and the square of magnetic-orbitals overlap (S^2) (see Computational Details). The results showed that as the K···O distance decreases, lower is the antiferromagnetic coupling and lower is the overlap of the magnetic orbitals (Figure 7b). However, an enhancement of the

magnetic coupling is observed for K···O distances smaller than 4 Å (Figure 7b). In Table S5 are listed the crystallographic K···O distances for **2** and **3**, with values of K1–$O23^{II}$ = 2.882(5)Å, K1–$O2^{II}$ = 2.852(4)Å, respectively. Based on the experimental K···O distances for the two systems, **2** should be more coupled than **3** (expected *J* = **2** > **3**). More non-covalent interactions should be taken into consideration to understand the experimental magnetic behaviour. Regarding the magnetic coupling and the Anderson-Weiss model [77], it is noteworthy that magnetic coupling affects the hyperfine interaction as the antiferromagnetic exchange increases; hence the hyperfine structure should be quenched. Therefore, as in our case, the magnetic coupling is affected by non-covalent interactions with the cation; it is plausible that the hyperfine structure will also be affected. Consistently, the poorly defined hyperfine structure was observed in systems **2** and **3** (Figure 5), that is, in compounds where the binuclear K–(O_2)–K unit includes O atoms that belong to vanadyl V^{IV}=O groups of different V_6-polyanions (Figure 2 and Table S5). On the other hand, the slightly defined hyperfine structure was observed for **1** that do not have K atoms in its crystalline packing. Consequently, we propose that the K–(O_2)–K units that connect two V_6-polyanion induce a decrease of the hyperfine interaction due to a change of the electronic density, affecting the magnetic coupling (Figure 7b). The lack of K-cations can explain the difference between the EPR spectra of the studied V_6-systems. Considering the importance of the electrostatic interactions present in the crystalline networks we evaluated, using the NCIPlot software [78], the non-covalent interactions of the *naked* $[V_6B_{20}O_{50}H_8]^{8-}$ cluster, and including 1,3-diapH^+ and K cations, that directly interact with the cluster in the networks (Figure S5). As expected, K cations (K···O interactions) have a significant incidence over the net electrostatic interactions, which can be associated with their influence to modulate the magnetic coupling of the V_6-rings. Besides, the minimum overlap between the magnetic orbitals agrees with maximum values of *J* at values of K···O_B between 3.5-4.0, indicating

that the larger cation effects on the overlap and the reinforcement of antiferromagnetic coupling are observed in the experimental range (Figure 7b).

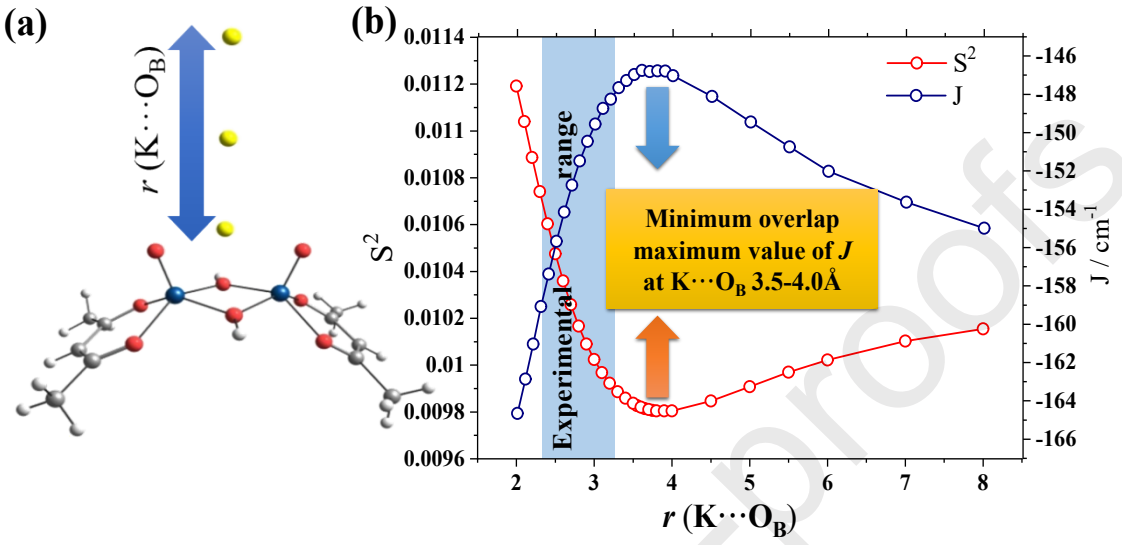

Figure 7. (a) Binuclear V^{IV} model with a K atom (yellow sphere) represented at different distances from the dioxo-{V^{IV}-V^{IV}} bridge (the K cation was fixed over the same plane of one of the oxygen-bridge atoms). (b) Square of magnetic-orbitals overlap (S^2) and magnetic coupling constant (J) as of the K···O distance function.

Regarding the magnetic coupling and the effect of potassium cation in the experimental range of distances for **2** and **3**, it is plausible to suggest that the decrease of the antiferromagnetic character (J_1, J_2, and J_3 fitted experimentally, Table S6) as the loss of hyperfine structure is due to the non-covalent interactions mainly with alkaline cations which affect the overlap of the V^{IV} magnetic orbitals.

Rationalization of the UV-Vis spectra based on TD-DFT

Theoretical calculations of the $[V_6B_{20}O_{50}H_8]^{8-}$ cluster using time-dependent methods were performed to comprehend the observed absorption bands (see Computational Details). The

comparison of the experimental UV-Vis spectrum of **3** with the computed excitations of the V_6-polyanion is shown in Figure 8. Three different levels of theory were tested, and a very similar distribution of the electronic excitations was achieved when the B3LYP and the B3PW91 functional were used. At the PBE0 level, an over-estimation of the excitation energies was obtained, displacing the higher energy bands below 300 nm. Calculations at the B3LYP level of theory reflect the best agreement with the experimental solid UV-Vis spectra (Figure 8); hence these results will be considered as a representative case. The results of the main electron excitation are summarized in Table 2. The three most important contributions for each transition show low values reaching up to 21%, indicating no dominant contribution, and a large set of molecular orbitals are involved in each transition. In this regard, a global landscape is needed to rationalize and give the assignment to each band. For this purpose, the hole-electron surfaces were calculated and fragmentally quantified based on percentual contribution (Table 2). The overlap between both surfaces indicates the local character of the transitions that occur in the same fragment. The polyanion was fragmented considering the V^{IV} metal centre, the terminal oxygen of the vanadyl groups ($O_{terminal}$), and the polyborate ligands ($[BO]_x$). Band I shows higher hole contributions coming from V3 and V4 with ~40%, whereas electron contribution remains at 34%, and overlap is ~37% of the total overlapped surface, indicating that a local process occurs. However, a non-neglectable part is transferred to O_t as observed in the electron contribution, which reaches 17%. On the other hand, band II presents contributions of all the V centres, showing a local character and a higher contribution of polyborate ligands that reach about ~19%. The third band (band III) corresponds to a local transition with higher contributions to hole and electron of V1, V2, V5, and V6 metal centres. The $\mathbf{\Sigma}O_{terminal}$ present a high contribution to electron surface, indicating a charge transfer $V \rightarrow O_t$ character that reaches 25%. Finally, band IV presents a charge transfer character, being V1, V3, V4, and V6, the higher contribution to hole while the electron contribution is centred on V2, V5, and $O_{terminal}$

fragments. This transition could be assigned to a MMCT between vanadium centres. The hole-electron surfaces were represented in Figure 9 to have a pictorial view of each excitation. The shape of the surfaces also allows us to infer univocally the kind of orbital involved in each transition. In the first case, band-I at 694 nm was assigned to local *d-d* transition due to $V^{IV}(xy) \rightarrow V^{IV}(xz,yz)$ showing a low *f* value since it corresponds to a Laporte forbidden transition. For band-II, the hole-electron surface indicates that the excitation at 510 nm corresponds to a *d-d* $V^{IV}(xy) \rightarrow V^{IV}(x^2\text{-}y^2)$ transition. The excitation obtained at 422 nm is due to *d-d* $V^{IV}(xy) \rightarrow V^{IV}(z^2)$ transitions for band-III. The analysis partially agrees with complexes based on vanadyl groups since band-I to band-III correspond to the expected electronic excitation of VO^{2+} fragment [79,80]. Band-IV was theoretically identified as a metal to metal charge transfer transition *MMCT*, that is, to a $V^{IV}(xy) \rightarrow V^{IV'}(xz,yz)$ transition, located at 307 nm. This band shows a higher intensity as expected for allowed charge transfer transitions. It is important to note the contribution of the O_t atoms in band-I, band-III, and band-IV, due to the symmetry shared between V and O atom of vanadyl group; contrarily, as observed for band-II, that corresponds to an excitation where O_t atom from vanadyl does not participate in the electron surface, because it does not share the symmetry. Finally, the theoretical assignment is supported by the intensity of the experimental bands, which is higher for the *MMCT*, and lower for the *d-d* type transitions, less permitted than the former.

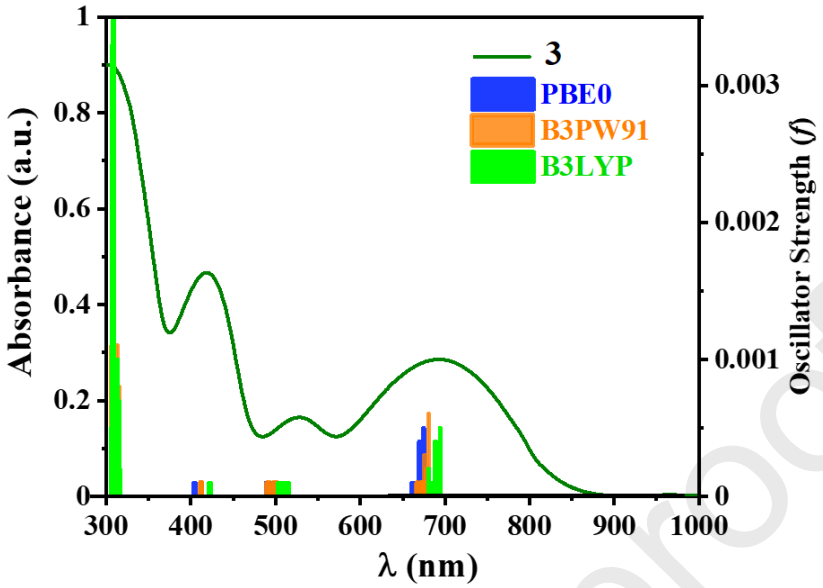

Figure 8. Theoretical electronic excitations (vertical lines) of the different tested functional, and the experimental spectra of **3** (green line).

Table 2. Theoretical parameters calculated for the main excitations of the V_6-system. Orbital and contributions for each excitation. H and L refers to HOMO and LUMO frontier molecular orbitals, respectively.

Band	λ (nm)	*f*	Orbitals	Surface	V1 (%)	V2 (%)	V3 (%)	V4 (%)	V5 (%)	V6 (%)	$\Sigma O_{terminal}$ (%)	$[BO]_x$ (%)	ΣVs (%)
I	694	0.0004	H-2→L+4 (13%)	Hole	1.0	2.2	39.6	39.6	2.2	1.0	0.6	13.8	85.6
			H →L+8 (12%)	Electron	0.8	2.2	34.2	34.2	2.2	0.8	17.3	8.4	74.3
			H-2→L+2 (11%)	Overlap	0.9	2.2	36.8	36.8	2.2	0.9	3.1	10.8	79.7
II	510	<0.0001	H-4→L+20 (18%)	Hole	16.7	7.0	19.4	19.4	7.0	16.7	0.5	13.2	86.3
			H-2→L+15 (18%)	Electron	15.1	6.4	18.4	18.4	6.4	15.1	0.4	19.9	79.6
			H-3→L+21 (10%)	Overlap	15.9	6.7	18.9	18.9	6.7	15.9	0.5	16.2	82.9
III	422	<0.0001	H-3→L+12 (21%)	Hole	27.2	14.8	1.1	1.1	14.8	27.2	0.5	13.4	86.1
			H-4→L+14 (10%)	Electron	20.6	11.1	0.8	0.8	11.1	20.6	24.4	10.8	64.8
			H-5→L+16 (10%)	Overlap	23.7	12.8	0.9	0.9	12.8	23.7	3.6	12.0	74.7
IV	308	0.0034	H-4→L+6 (12%)	Hole	21.1	5.1	17.0	17.0	5.1	21.1	0.8	12.8	86.4
			H-5→L+3 (15%)	Electron	7.4	26.9	3.0	3.0	26.9	7.4	18.5	6.8	74.6
			H-4→L+6 (12%)	Overlap	12.5	11.8	7.2	7.2	11.8	12.5	3.8	9.4	62.8

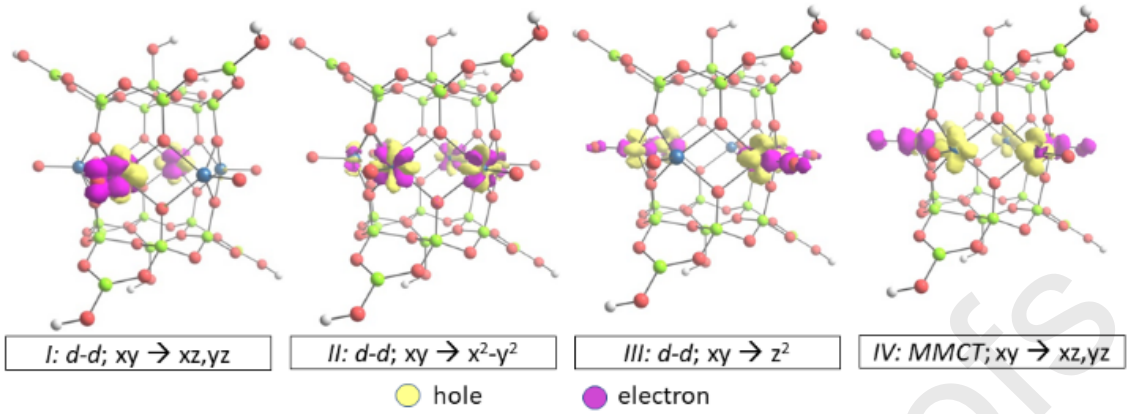

Figure 9. Molecular hole-electron surface for the most relevant excitation of the studied V_6-systems.

Conclusions

Three new *V_6-type* crystalline systems are reported and studied from a magnetic and spectroscopic viewpoint. In the reported systems, the magnitude of the antiferromagnetic coupling between the V^{IV}-V^{IV} of V_6-cores, is modulated by non-covalent interactions between K cations and the bridging oxygen atoms that link the V^{IV} in the V_6-rings. Based on a complete theoretical analysis, we show that the magnitude of the coupling is enhanced with K···O(-V^{IV}) electrostatic interactions at a distance smaller than 4 Å, associated with an increase of the magnetic-orbitals overlap as is expected for antiferromagnetic behaviours. Additionally, the hyperfine structure definition of the EPR spectra can also be explained in terms of these K···O non-covalent interactions since they can modify the electronic density and, therefore, modulate the overlap of the magnetic orbitals between the V^{IV} centres. In contrast, it is concluded that the optical properties of the systems are independent of the crystalline packing and the associated non-covalent interactions. Consequently, the optical properties are completely dominated only by local *d-d* and metal to metal charge transfer transitions that occur over the $\{V_6^{IV}O_{18}\}^{12-}$ central ring of the polyanions. Finally, for the first

time is demonstrated the importance of the crystalline packing in the magnetic properties of V_6-polyanions.

Acknowledgements

The authors acknowledge partial funding from FONDECYT 1201249 and Financiamiento Basal AFB180001. The international collaboration project LIA-M3 1027 is also acknowledged. Authors acknowledge FONDEQUIP EQM140060 and EQM130086. The calculations were performed at the supercomputing infrastructure of the National Laboratory for High Performance Computing, NLHPC (ECM-02), Universidad de Chile. KMB acknowledges to FONDECYT 3180509. KWA acknowledges to the postdoctoral positions 2018.021842VY _POSTDOC-USACH.

Appendix A. Supplementary data

CCDC 2115992-2115994 contains the supplementary crystallographic data for **1** – **3**. These data can be obtained free of charge via http://www.ccdc.cam.ac.uk/conts/retrieving.html, or from the Cambridge Crystallographic Data Centre, 12 Union Road, Cambridge CB2 1EZ, UK; fax: (+44) 1223-336-033; or e-mail: deposit@ccdc.cam.ac.uk.

References

[1] I.D. Williams, M. Wu, H.H.-Y. Sung, T.S.-C. Law, X.X. Zhang, Synthesis and properties of vanadoborate cluster materials, in: Contemp. Boron Chem., 2000: pp. 104–112. https://doi.org/10.1039/9781847550644-00104.

[2] P. Hermosilla-Ibáñez, K. Muñoz-Becerra, V. Paredes-García, E. Fur, E. Spodine, D.

Venegas-Yazigi, Structural and Electronic Properties of Polyoxovanadoborates Containing the [V12B18O60] Core in Different Mixed Valence States, Inorganics. 3 (2015) 309–331. https://doi.org/10.3390/inorganics3030309.

[3] H. Chen, Y. Deng, Z. Yu, H. Zhao, Q. Yao, X. Zou, J.E. Bäckvall, J. Sun, 3D open-framework vanadoborate as a highly effective heterogeneous pre-catalyst for the oxidation of alkylbenzenes, Chem. Mater. 25 (2013) 5031–5036. https://doi.org/10.1021/cm401400m.

[4] X. Liu, B. Guo, X. Sun, L. Zhang, H. Yuan, A New 3-D Open-Framework Zinc Borovanadate with Catalytic Potentials in α-Phenethyl Alcohol Oxidation, Molecules. 24 (2019) 531. https://doi.org/10.3390/molecules24030531.

[5] L. Zhang, X. Liu, F. Sun, J. Jian, X. Sun, D. Wu, H. Yuan, Proton conducting in a new vanadoborate with 3D structure through hydrogen bonding, J. Alloys Compd. 816 (2020) 152505. https://doi.org/10.1016/j.jallcom.2019.152505.

[6] X. Liu, J. Zhou, T.R. Amarante, F.A. Almeida Paz, L. Fu, Vanadoborates: cluster-based architectures, preparation and properties, Dalt. Trans. 50 (2021) 1550–1568. https://doi.org/10.1039/D0DT03820B.

[7] L. Zhang, X. Liu, L. Li, D. Zhang, X. Sun, H. Yuan, Facile proton conduction in a new 2D layered vanadoborate, J. Alloys Compd. 743 (2018) 136–140. https://doi.org/10.1016/j.jallcom.2018.01.342.

[8] I.D. Williams, M. Wu, H.H.Y. Sung, X.X. Zhang, J. Yu, An organotemplated vanadium(iv) borate polymer from boric acid ‘flux’ synthesis, [H2en]4[Hen]2[V6B22O53H8]·5H2O, Chem. Commun. (1998) 2463–2464. https://doi.org/10.1039/a805908j.

[9] C.J. Warren, J.T. Rijssenbeek, D.J. Rose, R.C. Haushalter, J. Zubieta, Hydrothermal synthesis and characterization of an unusual polyoxovanadium borate cluster: structure of Rb4[(VO)6{ {B10O16(OH)6} }2] · 0.5H2O, Polyhedron. 17 (1998) 2599–2605. https://doi.org/10.1016/S0277-5387(97)00395-1.

[10] Y.N. Cao, H.H. Zhang, C.C. Huang, Y.X. Sun, Y.P. Chen, W.J. Guo, F.L. Zhang, Synthesis and structural characterization of a new polyoxovanadium borate:(H3NCH2CH2NH3)(4)[(VO)(6)(B10O22)(2)] center dot (H3O)(7), CHINESE J. Struct. Chem. 24 (2005) 525–530.

[11] Q. Cai, B. Lu, J. Zhang, Y. Shan, Synthesis, structure and properties of (H2NCH2CH 2NH3)3 {(VO)6 [B10O 16 (OH)6]2} • 11H2O, J. Chem. Crystallogr. 38 (2008) 321–325. https://doi.org/10.1007/s10870-008-9325-y.

[12] X. Liu, J. Zhou, L. An, R. Chen, F. Hu, Q. Tang, Hydrothermal syntheses, crystal structures and characterization of new vanadoborates: The novel decorated cage cluster [V6B22O44(OH)10], J. Solid State Chem. 201 (2013) 79–84. https://doi.org/10.1016/j.jssc.2013.02.021.

[13] K. Muñoz-Becerra, P. Hermosilla-Ibáñez, E. Le Fur, O. Cador, V. Paredes-García, E. Spodine, D. Venegas-Yazigi, First Non-Centrosymmetric Deca-Vanadoborate with Borate Vacancies, Self-Assembled around a 1,3-Propanediammonium Cation, Cryst. Growth Des. 15 (2015) 2561–2564. https://doi.org/10.1021/acs.cgd.5b00102.

[14] M. Wu, T.S.C. Law, H.H.Y. Sung, J. Cai, I.D. Williams, Synthesis of elliptical vanadoborates housing bimetallic centers [Zn4(B2O4H2)(V10B28O74H8)]8? and [Mn4(C2O4)(V10B28O74H8)]10?, Chem. Commun. 4 (2005) 1827. https://doi.org/10.1039/b414697b.

[15] Y. Cao, H. Zhang, C. Huang, Q. Yang, Y. Chen, R. Sun, F. Zhang, W. Guo,

Synthesis, crystal structure and two-dimensional infrared correlation spectroscopy of a layer-like transition metal (TM)-oxalate templated polyoxovanadium borate, J. Solid State Chem. 178 (2005) 3563–3570. https://doi.org/10.1016/j.jssc.2005.09.017.

[16] C.J. Warren, R.C. Haushalter, D.J. Rose, J. Zubieta, A bimetallic main group oxide cluster of the oxovanadium borate system: (H3NCH2CH2NH3)4[(VO)12O4{B8O17(OH)4}2{Mn(H2O)2}2]·H2O, Inorganica Chim. Acta. 282 (1998) 123–129. https://doi.org/10.1016/S0020-1693(98)00187-X.

[17] Y. Cao, H. Zhang, C. Huang, Y. Chen, R. Sun, W. Guo, Hydrothermal synthesis and crystal structure of a novel 1D polyoxovanadium borate: (H3NCH2CH2NH3)3[(VO)12O4 {B8O17(OH)4}2{Na(H2O)}2]·(H3O)2(H2O)6.5, J. Mol. Struct. 733 (2005) 211–216. https://doi.org/10.1016/j.molstruc.2004.09.001.

[18] G. Li, H. Mei, S. Deng, Y. Sun, H. Hu, Y. Chen, H. Zhang, The Structure and Spectral Research on Mn2 [V12B16O52 (OH) 6](en) 2 (H3O) 6 (H2O) 5 (en= ethylenediamine), Spectrosc. Spectr. Anal. 31 (2011) 3026–3030. https://doi.org/10.3964/ j.issn.1000-0593(2011)11-3026-05.

[19] Y.-Q. Sun, G.-M. Li, Y.-P. Chen, A novel polyoxovanadium borate incorporating an organic amine ligand: synthesis and structure of [V12B16O50(OH)7(en)]7−, Dalt. Trans. 41 (2012) 5774. https://doi.org/10.1039/c2dt00018k.

[20] X. Liu, J. Zhou, H.-P. Xiao, C. Kong, H. Zou, Q. Tang, J. Li, Two new 3-D boratopolyoxovanadate architectures based on the [V12B16O50(OH)8]12− cluster with different metal linkers, New J. Chem. 37 (2013) 4077. https://doi.org/10.1039/c3nj00793f.

[21] J.T. Rijssenbeek, D.J. Rose, R.C. Haushalter, J. Zubieta, Novel Clusters of

Transition Metals and Main Group Oxides in the Alkylamine/Oxovanadium/Borate System, Angew. Chemie Int. Ed. English. 36 (1997) 1008–1010. https://doi.org/10.1002/anie.199710081.

[22] G.M. Li, H.X. Mei, X.Y. Chen, Y.P. Chen, Y.Q. Sun, H.H. Zhang, X.P. Chen, A porous organic-inorganic hybrid compound constructed from polyoxovanadium borate anions, dinuclear na sites and metal-organic units, Chinese J. Struct. Chem. 30 (2011) 785–792.

[23] J. Zhou, X. Liu, F. Hu, H. Zou, R. Li, X. Li, One novel 3-D vanadoborate with unusual 3-D Na–O–Na network, RSC Adv. 2 (2012) 10937. https://doi.org/10.1039/c2ra21635c.

[24] J. Zhou, X. Liu, F. Hu, H. Zou, X. Li, A new 1-D extended vanadoborate containing triply bridged metal complex units, Inorg. Chem. Commun. 25 (2012) 51–54. https://doi.org/10.1016/j.inoche.2012.07.050.

[25] P. Hermosilla-Ibáñez, P.E. Car, A. Vega, J. Costamagna, F. Caruso, J.-Y. Pivan, E. Le Fur, E. Spodine, D. Venegas-Yazigi, New structures based on the mixed valence polyoxometalate cluster [V12B18O60H6]n−, CrystEngComm. 14 (2012) 5604. https://doi.org/10.1039/c2ce25436k.

[26] P. Hermosilla-Ibáñez, W. Cañon-Mancisidor, J. Costamagna, A. Vega, V. Paredes-García, M.T. Garland, E. Le Fur, O. Cador, E. Spodine, D. Venegas-Yazigi, Crystal lattice effect on the quenching of the intracluster magnetic interaction in [V12B18O60H6](10-) polyoxometalate., Dalt. Trans. 43 (2014) 14132. https://doi.org/10.1039/c4dt01561d.

[27] P. Hermosilla-Ibáñez, J. Costamagna, A. Vega, V. Paredes-García, E. Le Fur, E. Spodine, D. Venegas-Yazigi, Coordination interactions in the crystalline lattice of

alkaline ions with the polyoxometalate [V 12 B 18 O 60 H 6] 10− ligand, J. Coord. Chem. 67 (2014) 3940–3952. https://doi.org/10.1080/00958972.2014.960407.

[28] P. Hermosilla-Ibáñez, J. Costamagna, A. Vega, V. Paredes-García, M.T. Garland, E. Le Fur, E. Spodine, D. Venegas-Yazigi, Protonated diamines as linkers in the supramolecular assemblies based on the [V12B18O60H6] polyoxovanadoborate anion, J. Struct. Chem. 55 (2015) 1453–1465. https://doi.org/10.1134/S0022476614080125.

[29] P. Hermosilla-Ibáñez, K. Wrighton-Araneda, L. Scarpetta-Pizo, W. Cañón-Mancisidor, M. Gutierrez-Cutiño, E. Le Fur, V. Paredes-García, D. Venegas-Yazigi, The origin of the electronic transitions of mixed valence polyoxovanadoborates [V 12 B 18 O 60]: from an experimental to a theoretical understanding, New J. Chem. (2019). https://doi.org/10.1039/C9NJ02549A.

[30] L. Zhang, Z. Shi, G. Yang, X. Chen, S. Feng, Hydrothermal Synthesis and X-Ray Single Crystal Structure of [Zn(en)2]6[(VO)12O6B18O39(OH)3]·13H2O, J. Solid State Chem. 148 (1999) 450–454. https://doi.org/10.1006/jssc.1999.8478.

[31] Z.H. Lin, H.H. Zhang, C.C. Huang, R.Q. Sun, Y.P. Chen, X.Y. Wu, Hydrothermal synthesis, crystal structure and properties of polyoxovanadium borate H-3 {[Cu (en)(2)](5)[(VO)(12) O6B18O42]{[B (OH)(3)](2) center dot 16H2O, Acta Chim. Sin. 62 (2004) 391–398.

[32] Z.H. Lin, H.H. Zhang, C.C. Huang, R.Q. Sun, Q.Y. Yang, X.Y. Wu, Hydrothermal synthesis and crystal structure of [Ni (en)(2)](6) H-2 [(VO)(12) O6B18O42] center dot 15H (2) O, Chinese J. Struct. Chem. 23 (2004) 83–86.

[33] Z. Lin, Q. Yang, H. Zhang, C. Huang, R. Sun, X. Wu, Hydrothermal Synthesis and Crystal Structure of (enH2)4Na4H3[(VO)12O6B18O42]·8H2O, Chinese J. Struct.

Chem. (2004) 590–595.

[34] L. Bin, W. Hong, Z. Li, D. Cheng-Yong, C. Qing-Hai, S. Yong-Kui, Hydrothermal Synthesis and Structure of K 3 Na 5 (H 2 NCH 2 CH 2 NH 3) 2 {(VO) 12 O 6 [B 3 O 6 (OH)] 6 }(H 2 O)·12H 2 O, Chinese J. Chem. 23 (2005) 137–143. https://doi.org/10.1002/cjoc.200590137.

[35] X. Liu, J. Zhou, The New Vanadoborate-supported Hexanuclear Zinc Complex [Zn(teta)]6[(VO)12O6B18O36(OH)6](H2O) · 8H2O, Zeitschrift Für Naturforsch. B. 66 (2011) 115–118. https://doi.org/10.1515/znb-2011-0202.

[36] X. Liu, J. Zhou, Z. Zhou, F. Zhang, Hydrothermal Syntheses and Crystal Structures of Two New Heteropolyoxovanadoborates Containing {(VO)12O6[B3O6(OH)]6(H2O)} Cluster, J. Clust. Sci. 22 (2011) 65–72. https://doi.org/10.1007/s10876-011-0359-5.

[37] K. Brown, P.E. Car, A. Vega, D. Venegas-Yazigi, V. Paredes-García, M.G.F. Vaz, R. a. Allao, J.Y. Pivan, E. Le Fur, E. Spodine, Polyoxometalate cluster [V12B18O60H 6] functionalized with the copper(II) bis-ethylenediamine complex, Inorganica Chim. Acta. 367 (2011) 21–28. https://doi.org/10.1016/j.ica.2010.11.045.

[38] T. Yamase, M. Suzuki, K. Ohtaka, Structures of photochemically prepared mixed-valence polyoxovanadate clusters: oblong [V18O44(N3)]14− , superkeggin [V18O42(PO4)]11− and doughnut-shaped [V12B32O84Na4]15 − anions, J. Chem. Soc. Dalt. Trans. 44 (1997) 2463–2472. https://doi.org/10.1039/a700916j.

[39] C.J. Warren, D.J. Rose, R.C. Haushalter, J. Zubieta, A New Transition Metal−Main Group Oxide Cluster in the Oxovanadium−Borate System: Hydrothermal Synthesis and Structure of (H 3 O) 12 [(VO) 12 {B 16 O 32 (OH) 4 } 2]·28H 2 O, Inorg. Chem. 37 (1998) 1140–1141. https://doi.org/10.1021/ic971452o.

[40] Bruker, COLLECT, Bruker AXS BV, 1997-2004, (n.d.).

[41] SAINTPLUS Version 6.02; Brucker AXS: Madison, WI, 1999., (n.d.).

[42] NONIUS, Kappa CCD Program Package: SCALEPACK, SORTAV; Nonius B.V. Delft, The Netherlands, 1999., (n.d.).

[43] Duisenberg, Schreurs, EVALCCD, 1990-2000., (n.d.).

[44] A.J.M. Duisenberg, Indexing in single-crystal diffractometry with an obstinate list of reflections, J. Appl. Crystallogr. 25 (1992) 92–96. https://doi.org/10.1107/S0021889891010634.

[45] SHELXTL Version 5.1, Brucker AXS: Madison, WI, 1998., (n.d.).

[46] G.M. Sheldrick, A short history of SHELX, Acta Crystallogr. Sect. A Found. Crystallogr. 64 (2008) 112–122. https://doi.org/10.1107/S0108767307043930.

[47] Sheldrick, G. M., SHELXL-97, Program for Crystal Structure Refinement; University of Göttingen, Germany, 1997., (n.d.).

[48] G.A. Bain, J.F. Berry, Diamagnetic Corrections and Pascal's Constants, J. Chem. Educ. 85 (2008) 532. https://doi.org/10.1021/ed085p532.

[49] B.J. and C.G. and J.A.P.M.W.W. G. E. S. M. J. Frisch, G. W. Trucks, H. B. Schlegel, T. V. M. A. Robb, J. R. Cheeseman, J. A. Montgomery, S. S. I. K. N. Kudin, J. C. Burant, J. M. Millam, G. S. J. Tomasi, V. Barone, B. Mennucci, M. Cossi, M. E. N. Rega, G. A. Petersson, H. Nakatsuji, M., GAUSSIAN 09 (Revision D.2), Gaussian, Inc., Pittsburgh, PA, USA, 2009., (2009).

[50] A.D. Becke, Density-functional thermochemistry. III. The role of exact exchange, J. Chem. Phys. 98 (1993) 5648–5652. https://doi.org/10.1063/1.464913.

[51] A.D. Becke, Density-functional exchange-energy approximation with correct asymptotic behavior, Phys. Rev. A. 38 (1988) 3098–3100. https://doi.org/10.1103/PhysRevA.38.3098.

[52] A. Schäfer, C. Huber, R. Ahlrichs, Fully optimized contracted Gaussian basis sets of triple zeta valence quality for atoms Li to Kr, J. Chem. Phys. 100 (1994) 5829–5835. https://doi.org/10.1063/1.467146.

[53] S. Grimme, S. Ehrlich, L. Goerigk, Effect of the damping function in dispersion corrected density functional theory, J. Comput. Chem. 32 (2011) 1456–1465. https://doi.org/10.1002/jcc.21759.

[54] A. V. Marenich, C.J. Cramer, D.G. Truhlar, Universal Solvation Model Based on Solute Electron Density and on a Continuum Model of the Solvent Defined by the Bulk Dielectric Constant and Atomic Surface Tensions, J. Phys. Chem. B. 113 (2009) 6378–6396. https://doi.org/10.1021/jp810292n.

[55] X. López, J.A. Fernández, S. Romo, J.F. Paul, L. Kazansky, J.M. Poblet, Are the solvent effects critical in the modeling of polyoxoanions?, J. Comput. Chem. 25 (2004) 1542–1549. https://doi.org/10.1002/jcc.20083.

[56] J.M. Poblet, X. López, C. Bo, Ab initio and DFT modelling of complex materials: towards the understanding of electronic and magnetic properties of polyoxometalates, Chem. Soc. Rev. 32 (2003) 297–308. https://doi.org/10.1039/B109928K.

[57] X. López, J.J. Carbó, C. Bo, J.M. Poblet, Structure, properties and reactivity of polyoxometalates: a theoretical perspective, Chem. Soc. Rev. 41 (2012) 7537. https://doi.org/10.1039/c2cs35168d.

[58] E. Runge, E.K.U. Gross, Density-Functional Theory for Time-Dependent Systems, Phys. Rev. Lett. 52 (1984) 997–1000. https://doi.org/10.1103/PhysRevLett.52.997.

[59] I. K. Burke and E. K. U. Gross, Density Functionals: Theory and Applications, Springer B, 2008.

[60] B. Weiner and S. B. Trickey, Advances in Quantum Chemistry, 1999.

[61] J.P. Perdew, J.A. Chevary, S.H. Vosko, K.A. Jackson, M.R. Pederson, D.J. Singh, C. Fiolhais, Atoms, molecules, solids, and surfaces: Applications of the generalized gradient approximation for exchange and correlation, Phys. Rev. B. 46 (1992) 6671–6687. https://doi.org/10.1103/PhysRevB.46.6671.

[62] J.P. Perdew, M. Ernzerhof, K. Burke, Rationale for mixing exact exchange with density functional approximations, J. Chem. Phys. 105 (1996) 9982–9985. https://doi.org/10.1063/1.472933.

[63] M. Ernzerhof, G.E. Scuseria, Assessment of the Perdew–Burke–Ernzerhof exchange-correlation functional, J. Chem. Phys. 110 (1999) 5029–5036. https://doi.org/10.1063/1.478401.

[64] C. Adamo, V. Barone, Toward reliable density functional methods without adjustable parameters: The PBE0 model, J. Chem. Phys. 110 (1999) 6158–6170. https://doi.org/10.1063/1.478522.

[65] T. Lu, F. Chen, Multiwfn: A multifunctional wavefunction analyzer, J. Comput. Chem. 33 (2012) 580–592. https://doi.org/10.1002/jcc.22885.

[66] L. Noodleman, Valence bond description of antiferromagnetic coupling in transition metal dimers, J. Chem. Phys. 74 (1981) 5737–5743. https://doi.org/10.1063/1.440939.

[67] L. Noodleman, E.R. Davidson, Ligand spin polarization and antiferromagnetic coupling in transition metal dimers, Chem. Phys. 109 (1986) 131–143. https://doi.org/10.1016/0301-0104(86)80192-6.

[68] Chemcraft - graphical software for visualization of quantum chemistry computations. https://www.chemcraftprog.com, (n.d.).

[69] B.F. Hoskins, F.D. Whillans, The geometry of pentacoordinate complexes, Coord. Chem. Rev. 9 (1973) 365–388. https://doi.org/10.1016/S0010-8545(00)82083-4.

[70] A.W. Addison, T.N. Rao, J. Reedijk, J. van Rijn, G.C. Verschoor, Synthesis, structure, and spectroscopic properties of copper(<scp>II</scp>) compounds containing nitrogen–sulphur donor ligands; the crystal and molecular structure of aqua[1,7-bis(N-methylbenzimidazol-2′-yl)-2,6-dithiaheptane]copper(<scp>II</scp>) pe, J. Chem. Soc., Dalt. Trans. (1984) 1349–1356. https://doi.org/10.1039/DT9840001349.

[71] I.D. Brown, D. Altermatt, Bond-valence parameters obtained from a systematic analysis of the Inorganic Crystal Structure Database, Acta Crystallogr. Sect. B Struct. Sci. 41 (1985) 244–247. https://doi.org/10.1107/S0108768185002063.

[72] K. Nakamoto, Infrared And Raman Spectra Of Inorganic And Coordination Compounds, Wiley Interscience Publications: Wisconsin, 1986.

[73] J. Selbin, Oxovanadium(IV) complexes, Coord. Chem. Rev. 1 (1966) 293–314. https://doi.org/10.1016/S0010-8545(00)80142-3.

[74] M.T. Pope, Polyoxometalate Chemistry From Topology via Self-Assembly to Applications, Luer Academic Publishers, New York, Boston, Dorrecht, London, Moscow, 2002. https://doi.org/10.1007/0-306-47625-8.

[75] M. Llunell, D. Casanova, J. Cirera, P. Alemany and S. Alvarez, SHAPE (2.1), Universitat de Barcelona, Barcelona, Spain, 2013, (n.d.).

[76] N.F. Chilton, R.P. Anderson, L.D. Turner, A. Soncini, K.S. Murray, PHI: A powerful new program for the analysis of anisotropic monomeric and exchange-coupled polynuclear d - and f -block complexes, J. Comput. Chem. 34 (2013) 1164–1175. https://doi.org/10.1002/jcc.23234.

[77] P.W. Anderson, P.R. Weiss, Exchange Narrowing in Paramagnetic Resonance, Rev. Mod. Phys. 25 (1953) 269–276. https://doi.org/10.1103/RevModPhys.25.269.

[78] J. Contreras-García, E.R. Johnson, S. Keinan, R. Chaudret, J.-P. Piquemal, D.N. Beratan, W. Yang, NCIPLOT: A Program for Plotting Noncovalent Interaction Regions, J. Chem. Theory Comput. 7 (2011) 625–632. https://doi.org/10.1021/ct100641a.

[79] C.J. Ballhausen, H.B. Gray, The Electronic Structure of the Vanadyl Ion, Inorg. Chem. 1 (1962) 111–122. https://doi.org/10.1021/ic50001a022.

[80] J.R. Winkler, H.B. Gray, Electronic Structures of Oxo-Metal Ions, in: 2011: pp. 17–28. https://doi.org/10.1007/430_2011_55.

Graphical abstract – Synopsis

The magnetic and electronic properties of crystalline packing of polyoxometalates of the $[V^{IV}_6B_{20}O_{50}H_8]^{8-}$ family were studied experimentally and theoretically. The magnetic V^{IV}-V^{IV} coupling is strongly dependent on the non-covalent interactions between K cations and polyanions, while the UV-Vis properties are dominated by MMCT and *d-d* transitions within the $\{V_6^{IV}O_{18}\}^{12-}$ chromophore.

Graphical abstract